J. Fluid Mech. (2022), *vol*. 949, A3, doi:10.1017/jfm.2022.759

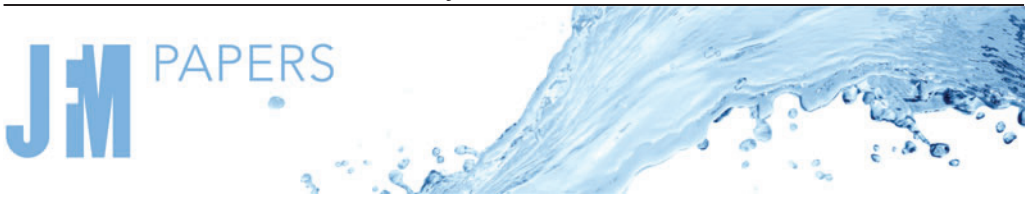

Experimental study of bubble competition and spike competition in Richtmyer–Meshkov flows

Yu Liang[1,2], **Lili Liu**[1,2] **and Xisheng Luo**[1,†]

[1]Advanced Propulsion Laboratory, Department of Modern Mechanics, University of Science and Technology of China, Hefei 230026, PR China

[2]NYUAD Research Institute, New York University Abu Dhabi, Abu Dhabi 129188, UAE

(Received 3 March 2022; revised 15 August 2022; accepted 29 August 2022)

Shock-tube experiments on various two-bubble and two-spike interfaces are performed to examine the dependence of bubble competition and spike competition on the initial spectra and density ratio of the interface. The differences in the influences of bubble competition and spike competition on the Richtmyer–Meshkov instability are highlighted for the first time. The bubble-competition effect is mainly dependent on the initial spectra of the two-bubble configuration. In contrast, the spike-competition effect is determined by both the initial spectra and density ratio. The extended buoyancy–drag model is adopted to explain the variation of the drag force imposed on the long-wavelength and short-wavelength structures as the initial conditions change. Based on the spectrum analysis, it is found that the constituent modes of two-bubble and two-spike interfaces have different contributions to the long-wavelength and short-wavelength perturbation growths. A generalised, nonlinear, analytical model is then established to quantify the bubble-competition effect and spike-competition effect considering arbitrary initial spectra and density ratio. The bubble-competition effect is believed to be stronger than the spike-competition effect at a high density ratio because it suppresses the high-frequency perturbation growth more evidently.

Key words: shock waves, nonlinear instability

1. Introduction

The Richtmyer–Meshkov (RM) instability (Richtmyer 1960; Meshkov 1969) occurs when an interface separating two fluids of different acoustic impedance is impulsively accelerated by a shock wave. Then bubbles (lighter fluids penetrating heavier ones) and spikes (heavier fluids penetrating lighter ones) arise, and turbulence might be finally

† Email address for correspondence: xluo@ustc.edu.cn

induced (Zhou *et al.* 2019). The RM instability plays an essential role in various industrial and scientific fields, such as inertial confinement fusion (ICF) (Lindl *et al.* 2014), supersonic combustion (Yang, Kubota & Zukoski 1993) and supernova explosions (Kuranz *et al.* 2018). For example, the RM instability enhances the mixing of hot fuel with cooler material in an ICF target, reducing and even eliminating the thermonuclear yield. However, in supersonic air-breathing engines, the RM instability increases the mixing area between fuel and air and thus enhances the combustion efficiency. Moreover, the RM instability shapes the filament structures in the Crab Nebula, the remnant of the historical supernova of 1054. Therefore, it is crucial to study the suppression or promotion of mixing induced by the RM instability due to its significant applications (Brouillette 2002; Ranjan, Oakley & Bonazza 2011; Zhou 2017*a*,*b*; Zhai *et al.* 2018; Livescu 2020; Zhou *et al.* 2021; Liang 2022).

A typical but simple RM instability is that on a single-mode interface, which has been extensively studied due to its fundamental significance (Richtmyer 1960; Meshkov 1969; Zhang & Sohn 1997; Sadot *et al.* 1998; Vandenboomgaerde, Gauthier & Mügler 2002; Niederhaus & Jacobs 2003; Jacobs & Krivets 2005; Mariani *et al.* 2008; Vandenboomgaerde *et al.* 2014; Zhang & Guo 2016; Liu *et al.* 2018; Zhang, Deng & Guo 2018; Mansoor *et al.* 2020). However, the initial perturbation in reality, such as that seeded on the surface between diverse materials in an ICF target, is essentially multi-mode with wavenumbers spanning many orders of magnitude (Miles *et al.* 2004). Past studies have shown that when the perturbation amplitude on a multi-mode RM unstable interface becomes comparable to its wavelength at the nonlinear regime, the competition between these multiple modes has a vital influence on instability development (Haan 1991; Ofer *et al.* 1996; Rikanati, Alon & Shvarts 1998; Sadot *et al.* 1998; Vandenboomgaerde *et al.* 2002; Niederhaus & Jacobs 2003; Balasubramanian, Orlicz & Prestridge 2013; Di Stefano *et al.* 2015*a*,*b*; Pandian, Stellingwerf & Abarzhi 2017; Elbaz & Shvarts 2018; Mohaghar *et al.* 2019). Our recent work (Luo *et al.* 2020; Liang *et al.* 2021*a*) further revealed that mode coupling is closely related to the initial spectra (including the wavenumber, phase and initial amplitude of constituent modes) and plays an essential role in RM flows from the very beginning if the initial amplitudes of the modes are large.

Moreover, at the turbulent regime, it is evident that perturbation increases following a self-similar law and is proportional to t^{θ} as a result of bubble competition and bubble merging (Alon *et al.* 1994, 1995; Dimonte & Schneider 2000). Recent studies indicated that the growth factor θ is dependent on the initial spectra (Zhou 2017*a*). For instance, an initial broadband perturbation leads to a larger θ than narrowband perturbation (Ramaprabhu, Dimonte & Andrews 2005; Thornber *et al.* 2010; Youngs 2013; Thornber 2016; Groom & Thornber 2020). Although the values of θ in many RM instability experiments and high-fidelity simulations, including the large collaborations of the θ-group (Thornber *et al.* 2017), have not been unified, it is widely accepted that the values of θ for bubbles and spikes are different due to different drag forces. For instance, the Atwood number (A, defined as $(\rho_2 - \rho_1)/(\rho_2 + \rho_1)$ with ρ_1 and ρ_2 denoting the density of the lighter fluid and heavier fluid, respectively) has a limited influence on θ for the bubble, but when $A \to 1$, θ for the spike is larger than its bubble counterpart (Youngs 1991; Dimonte & Schneider 2000; Cheng, Glimm & Sharp 2020). Therefore, the developments of instability of bubbles and spikes show different nonlinear behaviours in RM flows related to the initial spectra and density ratio.

Bubble competition is believed to have an important influence on the multi-mode RM unstable interface evolution at the nonlinear regime (Hecht, Alon & Shvarts 1994). In this process, larger bubbles, which have a higher velocity, rise and expand, while

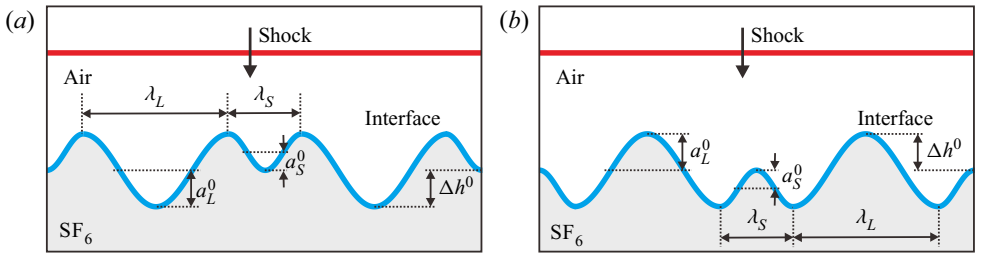

Figure 1. Initial configurations of two-bubble (*a*) and two-spike (*b*) RM instability experiments, where λ_L and λ_S denote the wavelengths of long-wavelength portions and short-wavelength portions, respectively; a_L^0 denotes the initial amplitude of the long-wavelength structure; a_S^0 denotes the initial amplitude of the short-wavelength structure; and Δh^0 denotes the initial height difference between the two bubbles or two spikes.

smaller bubbles shrink. In this study, we define the bubble-competition effect on the multi-mode RM instability as the deviation of the amplitude growths of bubbles from their single-mode counterpart. A simple configuration for a bubble-competition study is the so-called two-bubble configuration (see figure 1*a*) which is composed of adjacent bubbles initialised as neighbouring cosine waves of different wavelengths and amplitudes and is regarded as a classical multi-mode RM unstable interface. There are a few two-bubble RM instability studies focusing on bubble competition. Theoretically, based on the single-mode potential flow model (Layzer 1955), Hecht *et al.* (1994) derived a merger model for describing the bubble-competition effect on the Rayleigh–Taylor (RT) instability (Rayleigh 1883; Taylor 1950) and RM instability of a two-bubble interface with an infinite density ratio (i.e. $A = 1$) between incompressible fluids. Subsequently, Rikanati *et al.* (1998) considered the bubble-competition effect on the multi-mode RM instability in the limit of two fluids of similar densities (i.e. $A \to 0$) and proposed a statistical merger model based on the point vortices assumption (Jacobs & Sheeley 1996) to quantify the time-varying amplitude growths of the two bubbles. Rikanati *et al.* (1998) also found that the asymptotic bubble amplitude growth rate at $A = 0$ is different from that derived by Hecht *et al.* (1994) at $A = 1$ due to the added mass in the $A = 0$ case. Experimentally, Sadot *et al.* (1998) performed the first shock-tube experiment to investigate two-bubble competition and confirmed that the growth of the long-wavelength bubble is promoted but the short-wavelength bubble is suppressed in comparison with the single-mode RM instability. Recently, Guo *et al.* (2019) experimentally explored the RM instability of a chevron two-bubble interface containing sharp corners. It was found that as the initial size difference between the two bubbles increases, the bubble-competition effect occurs earlier, and the smaller bubble is affected more evidently. Numerically, Wadas & Johnsen (2020) utilised a high-order accurate discontinuous Galerkin code solving the Euler equations to simulate the RM instability of a two-bubble interface and observed vortex escape and bubble re-acceleration phenomena at the late nonlinear regime.

Although significant progress on the two-bubble RM instability has been made, the quantitative relation between the initial conditions and bubble competition is still unclear mainly because a general nonlinear theory for quantifying the bubble-competition effect considering arbitrary initial spectra and density ratio is absent. Moreover, compared with bubble-competition studies, spike competition has been rarely explored since it was challenging to distinguish the spike contours in previous experiments, and the growths of spikes of various sizes were considered to be independent at large A (Dimonte & Schneider 2000). However, the symmetry between bubbles and spikes is not broken at a low A (Niederhaus & Jacobs 2003). Furthermore, the Kelvin–Helmholtz instability

along the two sides of a spike promotes the effect of drag forces on the spike (Sharp 1984), which is more pronounced at a low A. Therefore, spike competition should exist, especially when the density ratio is limited, and should show a different behaviour from that of bubble competition in RM flows. In addition, the penetration of spikes in lighter fluids is generally more prominent than the penetration of bubbles in heavier fluids, which is adverse to the ignition of hot fuel in ICF. Overall, it is significant to explore the existence of spike competition, examine the differences between the bubble-competition effect and spike-competition effect on the RM instability and utilise these two competition mechanisms to reduce the mixing in ICF. These motivate the present study.

This study focuses on the bubble-competition effect on a two-bubble interface and the spike-competition effect on a two-spike interface. The existence of spike competition is reported for the first time. The soap film technique that has been widely utilised in our recent multi-mode RM instability studies (Liu *et al.* 2018; Liang *et al.* 2019, 2021*a*,*b*; Luo *et al.* 2019, 2020) is extended to form various two-bubble and two-spike interfaces. The contours of both bubbles and spikes are clearly distinguished, and evident quantitative data can be extracted. The differences between bubble competition and spike competition are highlighted. A nonlinear, analytical model is established to quantify the RM instability of two-bubble and two-spike interfaces with various spectra and density ratios.

2. Experimental configuration and method

The central part of a two-bubble (or two-spike) interface always consists of an initial short-wavelength (λ_S) bubble (or spike) flanked by two initial long-wavelength (λ_L) bubbles (or spikes), and the two sides are completed by partial short-wavelength bubbles (or spikes), as sketched in figure 1(*a*) (or figure 1*b*). The initial amplitudes of the long-wavelength bubble and spike (a_L^0) and the short-wavelength bubble and spike (a_S^0) are chosen such that the Richtmyer growth rates (Richtmyer 1960) of all bubbles and spikes are the same (i.e. $a_L^0/a_S^0 = \lambda_L/\lambda_S$). This, too, is consistent with previous two-bubble RM instability studies (Rikanati *et al.* 1998; Sadot *et al.* 1998; Guo *et al.* 2019; Wadas & Johnsen 2020).

The detailed physical parameters in all two-bubble cases (BC-) and two-spike cases (SC-) are listed in table 1, in which δ ($= \lambda_L/\lambda_S$) is the wavelength ratio of two bubbles and two spikes relative to the initial spectra. Overall, we investigate seven two-bubble interfaces and seven two-spike interfaces considering diverse δ and A, as listed in table 1. The Fourier expansions of two-bubble and two-spike interfaces with diverse δ are, respectively, expressed as

$$y = a_L^0[-C_1 \cos(kx) + \sum_{n>1} C_n \cos(nkx)], \quad n = 2, 3, 4 \ldots, \tag{2.1}$$

and

$$y = a_L^0[C_1 \cos(kx) - \sum_{n>1} C_n \cos(nkx)], \quad n = 2, 3, 4 \ldots, \tag{2.2}$$

where k ($= 2\pi/(\lambda_L + \lambda_S)$) is the wavenumber of the first-order mode of the two-bubble and two-spike configurations and C_n is the dimensionless coefficient of the nth-order mode. The first five modes are presented in figure 2 in the $\delta = 3.0$ case for instance. It is found that the long-wavelength structure and short-wavelength structure are formed by the peak or valley of various constituent modes. Furthermore, it is evident that although the two-bubble and two-spike interfaces are multi-mode ones with an infinite number of

Case	λ_L	λ_S	a_L^0	a_S^0	δ	Δh^0	MF	Δv	A	v_R	$\tau^*_{\Delta h}$
Single-mode	20.0	20.0	1.0	1.0	1.0	0	0.98	64.5	0.68	11.5	NA
BC-δ1.5A0.68	30.0	20.0	1.5	1.0	1.5	1.0	0.98	65.0	0.68	11.6	0.11
BC-δ2.0A0.68	40.0	20.0	2.0	1.0	2.0	2.0	0.98	66.4	0.68	11.8	0.08
BC-δ3.0A0.68	60.0	20.0	3.0	1.0	3.0	4.0	0.99	65.5	0.68	11.8	0.05
BC-δ6.0A0.68	60.0	10.0	3.0	0.5	6.0	5.0	0.98	65.5	0.68	11.7	0.12
BC-δ6.0A0.60	60.0	10.0	3.0	0.5	6.0	5.0	0.92	68.9	0.60	10.9	0.09
BC-δ6.0A0.50	60.0	10.0	3.0	0.5	6.0	5.0	0.82	71.3	0.50	9.3	0.08
BC-δ6.0A0.42	60.0	10.0	3.0	0.5	6.0	5.0	0.72	75.3	0.42	8.0	0.06
SC-δ1.5A0.68	30.0	20.0	1.5	1.0	1.5	1.0	0.98	65.0	0.68	11.6	0.16
SC-δ2.0A0.67	40.0	20.0	2.0	1.0	2.0	2.0	0.98	65.5	0.67	11.2	0.10
SC-δ3.0A0.68	60.0	20.0	3.0	1.0	3.0	4.0	0.98	67.8	0.68	12.0	0.07
SC-δ6.0A0.67	60.0	10.0	3.0	0.5	6.0	5.0	0.98	63.4	0.67	11.2	0.18
SC-δ6.0A0.56	60.0	10.0	3.0	0.5	6.0	5.0	0.88	69.8	0.56	10.2	0.14
SC-δ6.0A0.47	60.0	10.0	3.0	0.5	6.0	5.0	0.75	72.6	0.47	8.6	0.10
SC-δ6.0A0.37	60.0	10.0	3.0	0.5	6.0	5.0	0.66	77.0	0.37	7.4	0.07

Table 1. Physical parameters of single-mode, two-bubble and two-spike RM instability experiments, where $\delta = \lambda_L/\lambda_S$; Δh^0 denotes the initial height difference between two bubbles or two spikes; MF denotes the mass fraction of SF_6 in the test gas; Δv and A denote the post-shock flow velocity and Atwood number, respectively; v_R denotes the Richtmyer growth rate; and $\tau^*_{\Delta h}$ denotes the dimensionless criterion time when the competition mechanism occurs. The units for length, wavenumber and velocity are mm, m^{-1} and $m\,s^{-1}$, respectively.

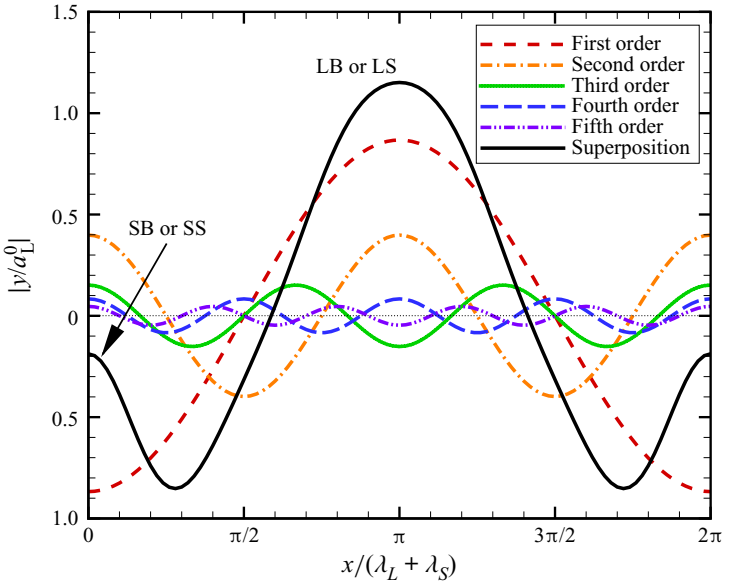

Figure 2. The superimposed interface by the first five modes when $\delta = 3.0$, where LB (or LS) denotes the long-wavelength bubble (or spike) and SB (or SS) denotes the short-wavelength bubble (or spike).

constituent modes, the interface configuration can be easily described by the superposition of the first several-order modes (see the solid black line in figure 2 as a superposition of the first five modes).

The values of C_n of the first five modes in different δ cases are shown in figure 3. It is found that the proportions of the high-frequency modes with orders higher than two are

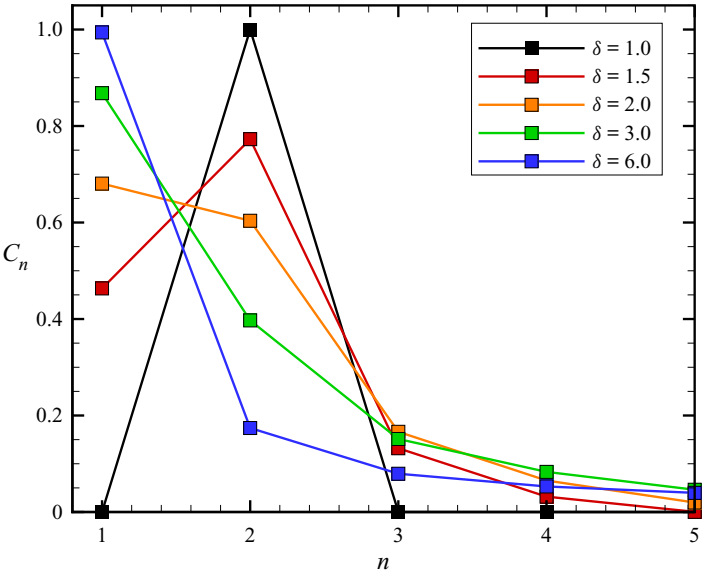

Figure 3. Coefficients of the nth-order mode in diverse δ cases.

limited and decrease as the order increases. Therefore, the first two modes dominate the morphologies of the two-bubble and two-spike interfaces. Moreover, as δ increases, C_1 increases, but C_2 decreases, indicating that the first-order mode becomes more significant and the second-order mode tends to be secondary, and the long-wavelength bubble (or spike) progressively dominates the two-bubble (or two-spike) interface. Overall, the two-bubble and two-spike interfaces are essentially quasi-dual-mode interfaces consisting of two dominant modes and an infinite number of residual higher-order modes.

The soap film technique is extended to generate a shape-controllable discontinuous interface to separate SF_6 from air, which can largely eliminate additional short-wavelength perturbations, diffusion layer and three-dimensionality (Liu *et al.* 2018; Liang *et al.* 2019, 2021*a*; Luo *et al.* 2020). Figure 4(*a*) shows that two transparent devices with an inner height of 7.0 mm and a width of 140.0 mm are first made using acrylic plates (3.0 mm in thickness). A groove (0.7 mm in thickness and 0.5 mm in width) with a two-bubble or two-spike shape is manufactured on each plate's inner side by a high-precision engraving machine. Then, two thin filaments (1.0 mm in thickness and 0.5 mm in width, as marked in green in figure 4) with the same shape are mounted into the grooves of the upper and lower plates, respectively, to produce desired constraints. Therefore, the bulging of the filament into the flow is less than 0.3 mm and has a negligible effect on the flow field. A small rectangular frame wetted by soap solution (78 % distilled water, 2 % sodium oleate and 20 % glycerine by mass) is pulled along the filaments, and a quasi-two-dimensional (2-D) soap film interface is immediately generated, as shown in figure 4(*b*). Subsequently, the auxiliary framework is gently inserted until it is completely connected to the corresponding device. After that, the framework with a soap film on its surface is slowly inserted into the test section of the shock tube.

To form an air–SF_6 interface, the air on the right-hand side of the soap film interface is partially replaced by SF_6. The surrounding gas is pure air, and the test gas is a mixture of SF_6 and air. The mass fractions of SF_6 in the test gas in various cases are different, as listed in table 1. The Mach number and velocity (v_s) of the incident shock wave are

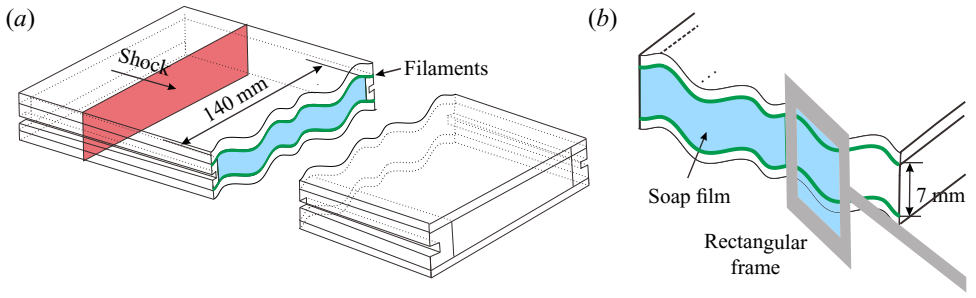

Figure 4. Schematic of soap film interface formation. (*a*) Two transparent devices with two-bubble shaped boundaries. (*b*) The soap film interface made by a rectangular frame.

1.18 ± 0.01 and 409 ± 3 m s^{-1}, respectively. The post-shock flow velocity (Δv) and A are listed in table 1. The ambient pressure is 101.3 kPa, and the temperature is 299.5 ± 1.0 K. The flow field is monitored by schlieren photography combined with a high-speed video camera (FASTCAM SA5, Photron Limited) with a frame rate of 62 500 frames per second and a spatial resolution of 0.4 mm pixel^{-1}.

3. Experimental observation

Figure 5(*a–e*) shows the schlieren images of the shocked two-bubble air–SF_6 interface evolution in five typical cases. For each two-bubble case, the moment when the shock contacts the downstream pole of the long-wavelength bubble is defined as the initial time ($t_B = 0$). In the example case BC-δ3.0A0.68, we can see that immediately after the transmitted shock leaves the interface, the shocked interface retains the initial interface shape (0.166 ms). Then, the symmetry between the bubble and spike in each cosine period is destroyed due to the development of the even-order modes (0.726 ms). Particularly, the second-order mode provides a constant acceleration for the bubble and the spike, which move in opposite directions, and, therefore, is the lowest order for asymmetry of the bubble and spike evolutions (Velikovich, Herrmann & Abarzhi 2014; Luo *et al.* 2019). Meanwhile, vortices appear on the spike due to the Kelvin–Helmholtz instability. Later, the competition and coalescence of large coherent structures drive the bubble-competition process (Oron *et al.* 2001; Srebro *et al.* 2003) as the high-order modes with orders larger than one develop, eventually leading to the spikes skewing towards the long-wavelength bubble (1.366 ms). As δ increases, the orientations of spikes become more pronounced as the long-wavelength bubble expands and the short-wavelength bubble is almost occupied by the long-wavelength bubble (case BC-δ6.0A0.68 at 1.360 ms, for instance). As A decreases, the density gradient is smaller, the interface contour is more indistinct and the interface velocity is larger (as in the example case BC-δ6.0A0.42 at 0.720 ms).

Figure 6(*a–e*) shows the schlieren images of the shocked two-spike air–SF_6 interface evolution in five typical cases. For each two-spike case, the moment when the shock contacts the upstream pole of the long-wavelength spike is defined as the initial time ($t_S = 0$). In the example case SC-δ3.0A0.68, as the two-spike interface evolves, the vortices roll up on the heads of all spikes, the stems of the long-wavelength spike and the short-wavelength spike become narrower and the orientations of all spikes maintain streamwise, agreeing well with the ordered, coherent pattern predicted by the group theory (Abarzhi 2008, 2010; Pandian *et al.* 2017). As δ increases, the vortices on the short-wavelength spike disappear (case SC-δ6.0A0.67 at 1.381 ms, for instance), and the

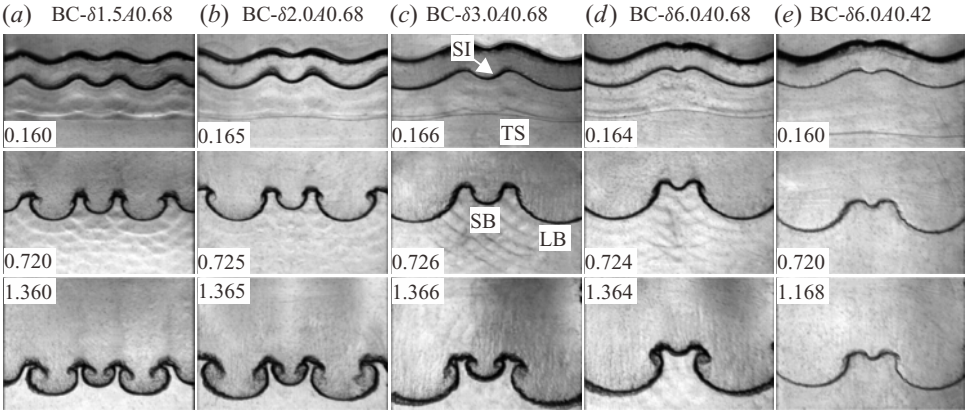

Figure 5. (*a–e*) Schlieren images of the shock-induced two-bubble interface evolutions, where TS denotes the transmitted shock, SI denotes the shocked interface and LB and SB denote the long- and short-wavelength bubbles. Shock wave moves from top to bottom. Numbers denote time in milliseconds, and similarly hereinafter.

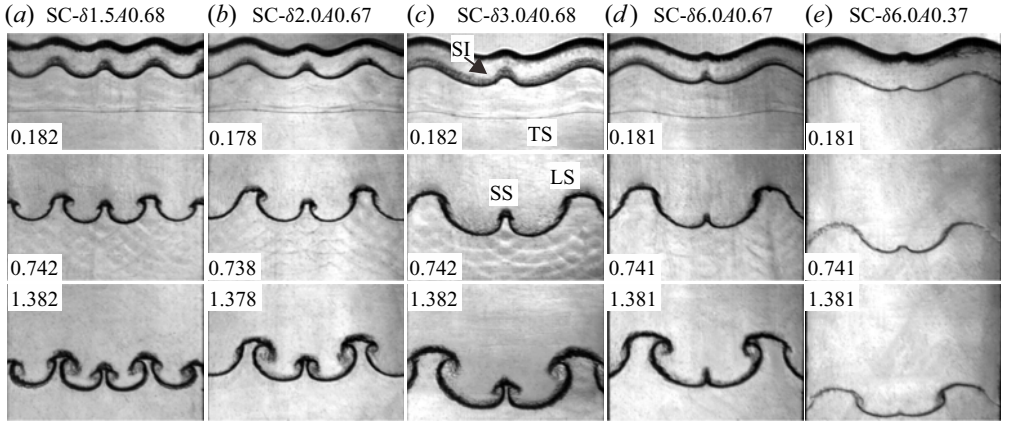

Figure 6. (*a–e*) Schlieren images of the shock-induced two-spike interface evolutions. LS and SS denote the long- and short-wavelength spikes.

bubbles on the two sides of the short-wavelength spike occupy its space. As A decreases, the short-wavelength spike is almost swallowed by the two-side bubbles completely (as in the example case SC-δ6.0A0.37 at 1.381 ms). Overall, the evolving two-spike interface shows a significantly different morphology from its two-bubble counterpart.

4. Quantitative results

The amplitude histories for the two bubbles (or spikes) of the two-bubble (or two-spike) interface are quantitatively compared. To distinguish the bubble amplitude from its spike counterpart, the movement of the unperturbed interface obtained by the one-dimensional gas dynamics theory (Drake 2018) with the initial conditions of each case is provided as a moving reference. The amplitudes of the long-wavelength bubble (a_{LB}), short-wavelength bubble (a_{SB}), long-wavelength spike (a_{LS}) and short-wavelength spike (a_{SS}) are defined as the distances between the tips of bubbles or spikes with the moving references, as

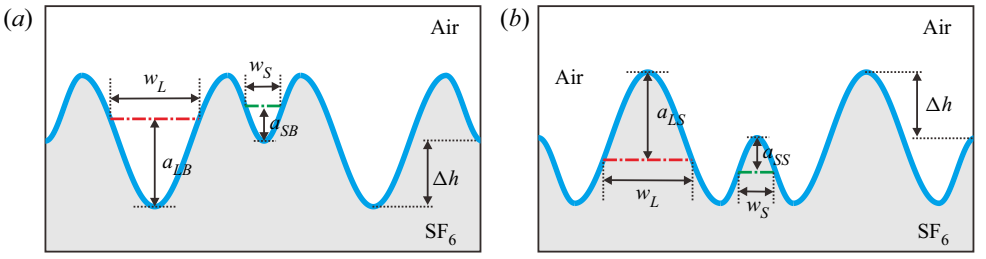

Figure 7. Sketches of the characteristic lengths measured in the two-bubble (*a*) and two-spike (*b*) RM instability experiments, where a_{LB}, a_{SB}, a_{LS} and a_{SS} denote the time-varying amplitudes of the long-wavelength bubble, short-wavelength bubble, long-wavelength spike and short-wavelength spike, respectively; w_L and w_S denote the time-varying widths of the long-wavelength and short-wavelength structures, respectively; and Δh denotes the time-varying height difference between the two bubbles or two spikes. Red and green dashed-dot lines represent the moving references calculated by the one-dimensional gas dynamics theory for the long-wavelength and short-wavelength structures, respectively.

sketched in figure 7. The time-varying dimensionless amplitudes of a_{LB}, a_{SB}, a_{LS} and a_{SS} are calculated, as shown in figure 8.

For two-bubble cases, time is scaled as $\tau_B = 2\pi v_R t_B/\lambda_L$ (or $\tau_B = 2\pi v_R t_B/\lambda_S$) for the long-wavelength (or short-wavelength) bubble, where v_R $(= 2\pi Z a_L^0 \Delta v A/\lambda_L)$ denotes the Richtmyer growth rate (Richtmyer 1960), and Z $(= 1 - \Delta v/v_s)$ denotes the shock compression factor; amplitude is scaled as $\eta_B = 2\pi(a_{LB} - Z a_L^0)/\lambda_L$ (or $\eta_B = 2\pi(a_{SB} - Z a_S^0)/\lambda_S$) for the long-wavelength (or short-wavelength) bubble. For two-spike cases, time is scaled as $\tau_S = 2\pi v_R t_S/\lambda_L$ (or $\tau_S = 2\pi v_R t_S/\lambda_S$) for the long-wavelength (or short-wavelength) spike; amplitude is scaled as $\eta_S = 2\pi(a_{LS} - Z a_L^0)/\lambda_L$ (or $\eta_S = 2\pi(a_{SS} - Z a_S^0)/\lambda_S$) for the long-wavelength (or short-wavelength) spike. The values of v_R are listed in table 1. To highlight the effects of bubble competition and spike competition, the RM instability of a single-mode interface is shown with black diamond symbols in figures 8(*a*) and 8(*b*) for comparison. The Richtmyer growth rates of the two bubbles are the same, and the short-wavelength bubble reaches the asymptotic linear growth rates earlier than its long-wavelength bubble counterpart due to its short startup time (Lombardini & Pullin 2009), and, therefore, the short-wavelength bubble grows slightly more than the long-wavelength bubble at the very early times, as shown in the zoomed inset of figure 8(*a*).

Four observational findings, in particular, are noteworthy. First, the amplitudes of two bubbles and two spikes experience a linear growth at an early time. However, the criterion time between the linear and nonlinear regimes of the RM instability of the two-bubble interface (about 0.5) is less than that of its two-spike counterpart (around 1.0). Because the development of a bubble is suppressed by the second- and third-order harmonics generated by the bubble itself (Velikovich & Dimonte 1996; Zhang & Sohn 1997; Vandenboomgaerde *et al.* 2002; Nishihara *et al.* 2010; Velikovich *et al.* 2014), whereas the development of a spike is promoted by the second-order harmonics but suppressed by the third-order harmonics produced by the spike itself, the spike amplitude growth shows a more prolonged linear regime than its bubble counterpart.

Second, the bubble competition and spike competition suppress the nonlinear growths of the short-wavelength bubble and spike, respectively. However, the suppressions imposed by the bubble competition and spike competition are different. For instance, a_{SB} saturates in the BC-δ1.5*A*0.68 case after dimensionless time 3.5, but a_{SS} still grows in the

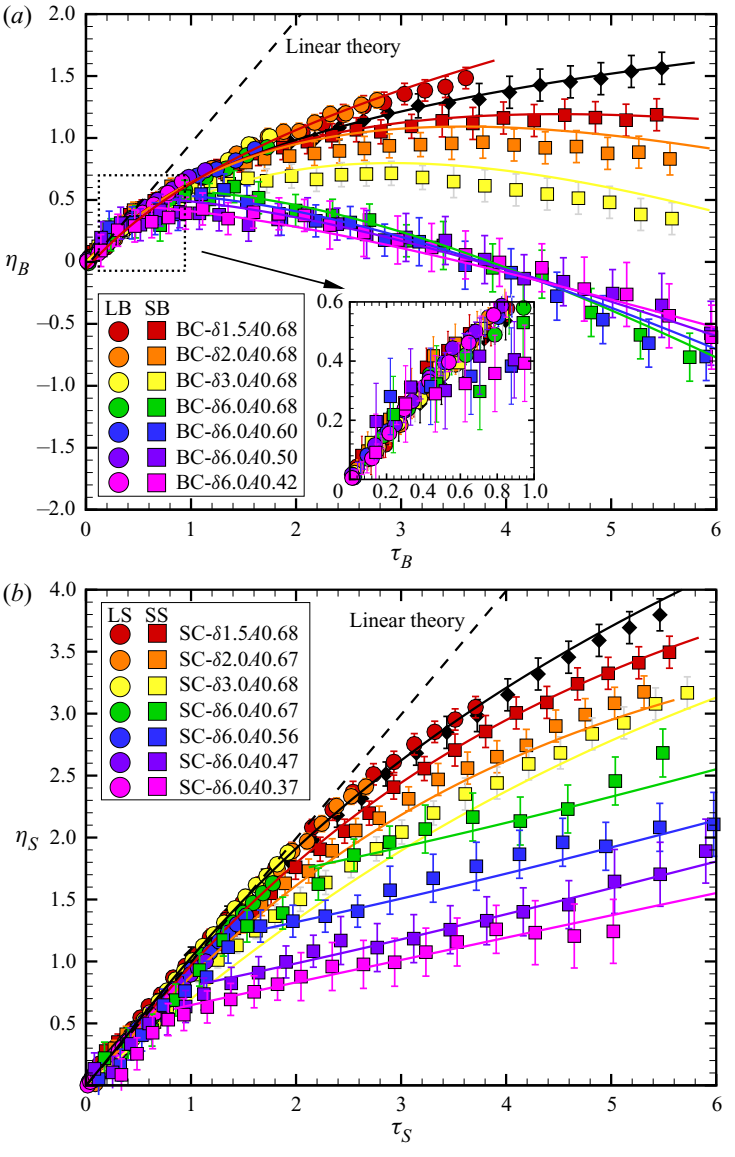

Figure 8. The time-varying dimensionless (*a*) two-bubble amplitudes and (*b*) two-spike amplitudes. Symbols represent the experiments and solid lines with colours corresponding to symbols represent the theoretical prediction calculated with (4.12).

SC-δ1.5A0.68 case, indicating that the effects of bubble competition and spike competition on the RM instability are different.

Third, the bubble-competition effect on the short-wavelength bubble is dominated by the initial spectra of the two-bubble configuration but is weakly dependent on the density ratio. In contrast, the spike-competition effect on the short-wavelength spike is determined by both the initial spectra and density ratio. As δ increases, both a_{SB} and a_{SS} decrease evidently, indicating that both the bubble-competition effect and spike-competition effect are more substantial. However, as A decreases, a_{SB} increases slightly, but a_{SS} decreases

obviously, indicating that bubble competition and spike competition have different dependencies on the density ratio.

Fourth, compared with the single-mode RM instability, the bubble competition slightly promotes the nonlinear amplitude growths of the long-wavelength bubble. In contrast, the spike competition has a limited influence on the long-wavelength spike. Overall, the influences of bubble competition and spike competition on the long-wavelength structures and short-wavelength structures are different.

In this study, we explain the observational findings in two ways. One is based on the physics-related buoyancy–drag model and the other is according to the modal analysis of the interface contour.

First, the buoyancy–drag model is a simple physics model for describing the RT and RM instabilities (Cheng, Glimm & Sharp 2000; Dimonte 2000; Oron *et al.* 2001; Srebro *et al.* 2003; Youngs & Thornber 2020). Briefly, the buoyancy–drag model is an equation of motion that balances inertia, buoyancy and Newtonian drag forces. Here, we adopt the extended buoyancy–drag model covering all instability regimes (Dimonte 2000; Oron *et al.* 2001; Youngs & Thornber 2020):

$$(\rho_i + C_a\rho_{i'})\frac{\mathrm{d}v_i}{\mathrm{d}t} = (\rho_2 - \rho_1)g - C_d\rho_{i'}\frac{v_i^2}{\lambda_i}, \tag{4.1}$$

with $i = 1$ for the bubble and $i = 2$ for the spike, $i' = 3 - i$, v_i ($= \mathrm{d}a_i/\mathrm{d}t$) is the amplitude growth rate, λ_i is the perturbation wavelength, g is the acceleration, C_a is an added mass coefficient and C_d is a drag coefficient. Assuming that both C_a and C_d are independent of A (Oron *et al.* 2001; Srebro *et al.* 2003), $C_a = 2$ for 2-D perturbations and 1 for three-dimensional perturbations, and $C_d = 6\pi$ for 2-D perturbations and 2π for three-dimensional perturbations. By introducing a self-similar geometric parameter β_i ($= a_i/\lambda_i$), equation (4.1) is rewritten as

$$\frac{\mathrm{d}v_i}{\mathrm{d}t} = \frac{\rho_1 + \rho_2}{\rho_i + C_a\rho_{i'}}Ag - C_d\frac{\rho_{i'}\beta_i}{\rho_i + C_a\rho_{i'}}\frac{v_i^2}{a_i}. \tag{4.2}$$

For the RM instability with an impulsive acceleration ($g = 0$), v_i and t are scaled as (Cheng, Glimm & Sharp 2002; Cao, Chow & Fong 2011)

$$v_i^* = \frac{v_i}{\sqrt{Aa_i}}, \quad \mathrm{d}t^* = \sqrt{\frac{A}{a_i}}\mathrm{d}t. \tag{4.3a,b}$$

Substituting equation (4.3*a*,*b*) into (4.2), we have

$$\frac{\mathrm{d}v_i^*}{\mathrm{d}t^*} = -\frac{1}{2} + \frac{C_d\rho_{i'}\beta_i v_i^{*2}}{\rho_i + C_a\rho_{i'}}. \tag{4.4}$$

Integrating equation (4.4), the solution for the RM instability is

$$a_i = a_i^o\left[1 + \frac{v_i^o}{a_i^o\theta_i}(t - t^o)\right]^{\theta_i}, \tag{4.5}$$

with a_i^o and v_i^o denoting the amplitude and the amplitude growth rate at t^o (i.e. arbitrary time at the self-similar regime), respectively, and

$$\theta_i = \frac{\rho_i + C_a\rho_{i'}}{\rho_i + (C_a + \beta_i C_d)\rho_{i'}}. \tag{4.6}$$

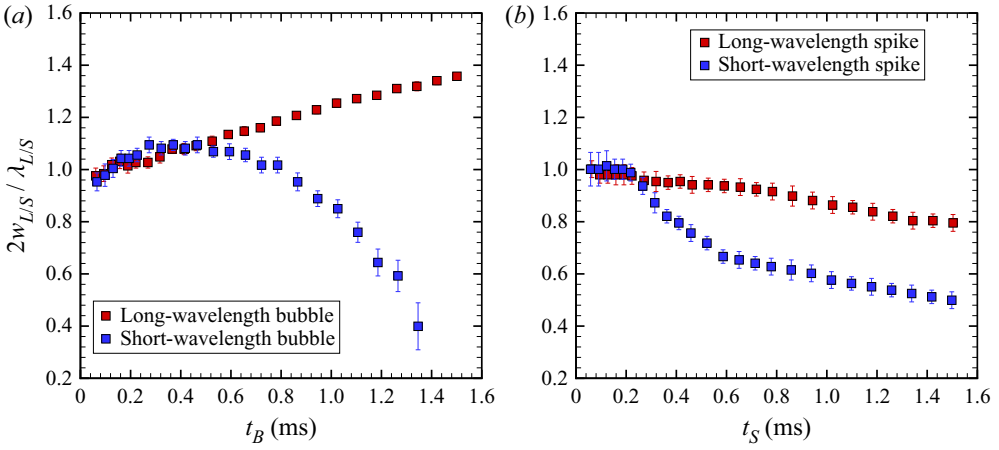

Figure 9. The time-varying wavelengths of the long-wavelength and short-wavelength structures in the (*a*) BC-δ3.0A0.68 case and (*b*) SC-δ3.0A0.68 case.

Therefore, the expressions for θ_1 and θ_2, respectively, are

$$\theta_1 = \frac{1}{1 + a_1 C_d/[\lambda_1(C_a + 1/R)]} \tag{4.7}$$

and

$$\theta_2 = \frac{1}{1 + a_2 C_d/[\lambda_2(R + C_a)]}, \tag{4.8}$$

with $R = \rho_2/\rho_1$. Notably, a_1 and λ_1, a_2 and λ_2 are instantaneous values in (4.7) and (4.8), respectively. In this study, the widths of the long-wavelength structure (w_L) and the short-wavelength structure (w_S) are defined as the spanwise lengths of the moving references within a period of the structure, as sketched in figure 7.

For the two-bubble studies, the time-varying widths of the long-wavelength bubble and short-wavelength bubble in the BC-δ3.0A0.68 case are measured from the experiments and shown in figure 9(*a*), for instance. It is evident that the dimensionless w_L is larger than 1.0 and progressively increases, whereas the dimensionless w_S is lower than 1.0 and gradually decreases. In other words, the long-wavelength bubble expands while the short-wavelength bubble shrinks and, therefore, λ_1 increases for the long-wavelength bubble and decreases for the short-wavelength bubble in (4.7). From a physical perspective, the drag per unit volume (i.e. C_d/λ_1) of the long-wavelength bubble is reduced, but that of the short-wavelength bubble is increased. As a result, θ_1 is increased for the long-wavelength bubble but suppressed for the short-wavelength bubble on comparing with the single-mode RM unstable bubble.

For the two-spike studies, the time-varying widths of the long-wavelength spike and short-wavelength spike in the SC-δ3.0A0.68 case are shown in figure 9(*b*), for instance. It is found that the dimensionless w_S is lower than 1.0 and progressively decreases. Although the dimensionless w_L also decreases, the decrease of w_L is limited (less than 20 %) during the whole experimental time. In other words, the two-side bubbles have different influences on the two spikes, leading to the competition between the two spikes. The two-side bubbles of a two-spike interface swallow the space of the short-wavelength spike but have a limited influence on the long-wavelength spike and, therefore, the drag per unit volume (i.e. C_d/λ_2) of the short-wavelength spike is increased while that of the

long-wavelength spike is limitedly influenced. As a result, θ_2 is kept or slightly suppressed for the long-wavelength spike but evidently suppressed for the short-wavelength spike on comparing with the single-mode RM unstable spike.

Moreover, as A (or R) increases, it is found that the drag force imposed by heavier fluids on the bubble (i.e. C_dR) increases, whereas the drag force imposed by lighter fluids on the spike (i.e. C_d/R) decreases. Therefore, θ_1 decreases, but θ_2 increases. In addition, due to $1/R < 1 \leq C_a$ in (4.7) and $R \geq C_a$ in (4.8), the variation of R has a larger influence on θ_2 than on θ_1. Therefore, the spike-competition effect is more dependent on the density ratio than the bubble-competition effect. As a result, the spike competition is dependent on both the initial spectra and density ratio. Still, the bubble-competition effect depends more on the initial spectra than the density ratio.

The growth trends of both the long-wavelength and short-wavelength structures can be qualitatively explained based on the buoyancy–drag model and experimental observation. However, it is challenging to adopt the buoyancy–drag model to quantify the time-varying amplitude growths of the two bubbles and two spikes since the quantitative relation between the self-similar factor β_i, i.e. the ratio of a_i to λ_i, with the initial conditions remains an open problem (Oron *et al.* 2001; Zhou, Zhang & Tian 2018). Previous theoretical and experimental studies have identified inconsistent values of β_1, including $\approx$2.5 (Mikaelian 1989), $\approx 4/(1+A)$ (Dimonte & Schneider 2000; Dimonte *et al.* 2004), $\approx 0.5/(1+A)$ in 2-D RT flow (Alon *et al.* 1994, 1995), and $\approx 0.26-0.4$ in 2-D RM flow (Hecht *et al.* 1994; Rikanati *et al.* 1998). The expression for β_2 is still unknown.

Second, according to the Fourier expansions of the two-bubble and two-spike configurations (see figure 2), the phase of the first-order mode is opposite to the phases of the higher-order modes at the tips of the short-wavelength bubble and spike (i.e. $x = 0$), whereas the phase of the first-order mode is the same as the phases of even-order modes at the tips of the long-wavelength bubble and spike (i.e. $x = \pi/k$). As a result, on the one hand, the first-order mode suppresses but the higher-order modes promote the amplitude growths of the short-wavelength bubble and spike; while the first-order mode and even-order modes (e.g. second- and fourth-order modes) promote but the higher odd-order modes (e.g. third- and fifth-order modes) suppress the amplitude growths of the long-wavelength bubble and spike.

Referring to the findings in figures 8(a) and 8(b), it is evident that the RM instability of short-wavelength structures is suppressed by the lowest frequency mode. In other words, the spanwise flow field suppresses the short-wavelength perturbation growths. As δ increases, the proportion of the first-order mode in the initial interfacial morphology is larger. Therefore, the suppression imposed by the lowest frequency mode on the short-wavelength perturbation growth is larger. Moreover, the RM instability of the long-wavelength structures is decided by the competition between the promotion imposed by the first-order mode and even-order modes with the suppression induced by the higher odd-order modes. Our experiments demonstrate that the RM instability of the long-wavelength bubble is slightly promoted, indicating that the promotion induced by the first-order mode and even-order modes is larger than the suppression imposed by the higher odd-order modes. Differently, the RM instability of the long-wavelength spike is influenced limitedly, indicating that a balance between the competition of the constituent modes is achieved for the long-wavelength spike. Overall, the constituent modes of the two-bubble and two-spike interfaces significantly influence the bubble competition and spike competition, especially the RM instability of short-wavelength structures.

Since the two-bubble and two-spike interfaces consist of two dominant modes and an infinite number of secondary modes, it is significant to examine the couplings between these multiple modes. The captured interface morphology is distinct such that the interface contours in all cases can be extracted by an image-processing program, as indicated by the insets in figures 10(*a*) and 10(*b*). The mean y coordinate in each image is taken as the average position of the local interface. Spectrum analysis is then performed on the extracted interface displacement on the certain x–y plane before the interface becomes multi-valued, and the time-varying magnitudes of the first five modes (a_n) are acquired, as shown in figure 10(*a*) for the BC-δ3.0A0.68 case and figure 10(*b*) for the SC-δ3.0A0.68 case, for instance. It is evident that the constituent modes of a two-bubble interface grow in a direction opposite to that of its two-spike interface counterpart. To highlight the mode coupling effect on the development of each constituent mode, the potential flow model, proposed by Dimonte & Ramaprabhu (2010) (DR model) for predicting the 2-D single-mode RM instability considering various amplitude-to-wavelength ratios, shock intensities and density ratios, is modified to quantify the magnitude growth rate of the nth mode ($v_n(t)$) without couplings as

$$v_n(t) = [v_{nB}(t) + v_{nS}(t)]/2, \tag{4.9}$$

with the bubble/spike magnitude growth rate of the nth mode, $v_{nB/nS}(t)$, calculated by

$$v_{nB/nS}(t) = \frac{(-1)^i v_n^0[1 + (1 \mp A)nkv_n^0 t_{B/S}]}{1 + G_{B/S}nkv_n^0 t_{B/S} + (1 \mp A)F_{B/S}(nkv_n^0 t_{B/S})^2}, \tag{4.10}$$

in which $i = 1$ for the first-order mode and $i = 0$ for the other modes of a two-bubble interface; and $i = 0$ for the first-order mode and $i = 1$ for the other modes of a two-spike interface, and

$$\left.\begin{array}{c} v_n^0 = Znk\Delta vAC_n a_L^0, \\ G_{B/S} = \dfrac{4.5 \pm A + (2 \mp A)ZnkC_n a_L^0}{4}, \\ F_{B/S} = 1 \pm A. \end{array}\right\} \tag{4.11}$$

The upper (or lower) sign of $\pm$ and $\mp$ applies to the bubble (or spike) in all equations of this work. The predictions of the modified DR model, as shown in figures 10(*a*) and 10(*b*) with colour lines corresponding to the symbols, agree well with the experiments, especially the two dominant modes with the lowest frequencies. The agreement indicates that the mode coupling can be reasonably neglected, which is not surprising since each constituent mode satisfies the small-perturbation prerequisite (i.e. $nkC_n a_L^0 \ll 1$) in this study and the coupling among modes is limited at the weakly nonlinear regime (Luo *et al.* 2020; Liang *et al.* 2021*a*).

Furthermore, a simple, analytical nonlinear model is established to quantify the RM instability of the two-bubble and two-spike interfaces based on the modified DR model. According to the tip positions of the long-wavelength and short-wavelength structures, a universal expression for the nonlinear amplitude growth rates of the long-wavelength bubble ($v_{LB}(t)$) and spike ($v_{LS}(t)$) and the short-wavelength bubble ($v_{SB}(t)$) and spike ($v_{SS}(t)$) is

$$v_{LB/LS/SB/SS}(t) = \sum_n \frac{(-1)^j v_n^0[1 + (1 \mp A)nkv_n^0 t_{B/S}]}{1 + G_{B/S}nkv_n^0 t_{B/S} + (1 \mp A)F_{B/S}(nkv_n^0 t_{B/S})^2}, \tag{4.12}$$

in which $n = 1, 2, 3, \ldots$; $j = 0$ for the first-order mode and even-order modes and $j = 1$ for the higher odd-order modes of the long-wavelength bubble and spike; $j = 1$ for the

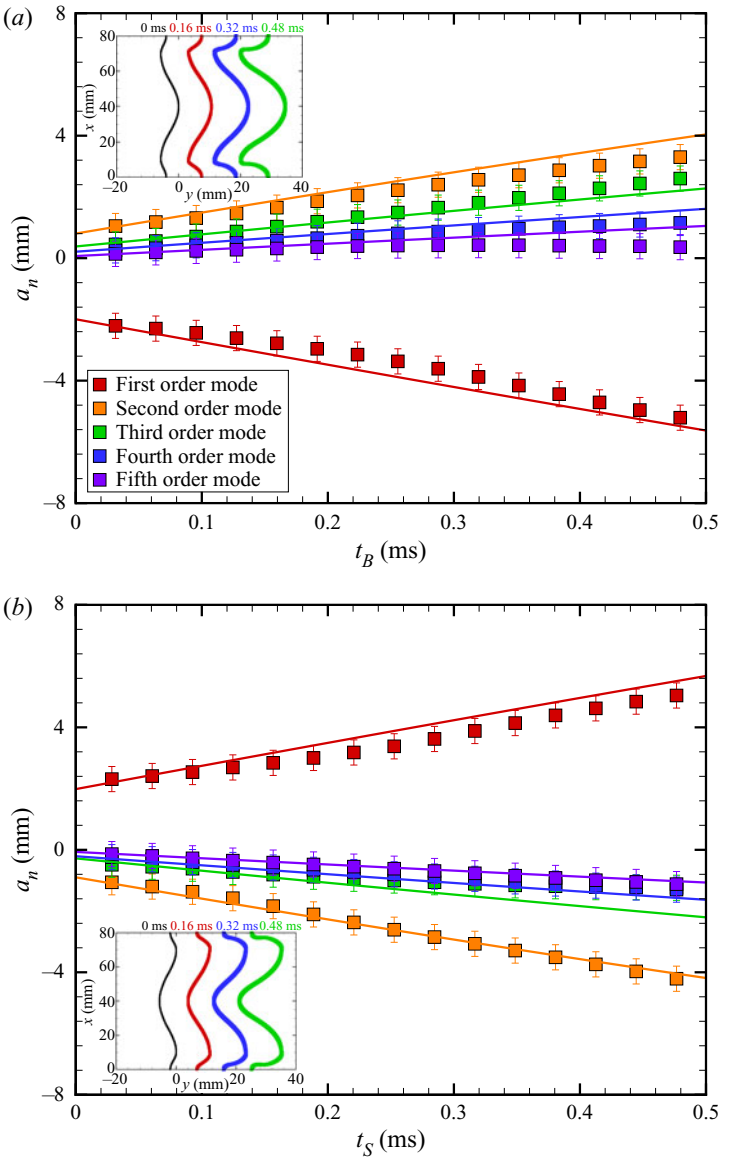

Figure 10. The time-varying magnitudes of the first five modes obtained from the (*a*) BC-δ3.0A0.68 case and (*b*) SC-δ3.0A0.68 case. The solid lines represent the predictions of the modified DR model (equations (4.9)–(4.11)). The insets show the interface contours for the spectrum analysis.

first-order mode and $j = 0$ for the other modes of the short-wavelength bubble and spike. The predictions of the nonlinear model with consideration of the sum of the first five modes are presented with corresponding colour lines in figures 8(*a*) and 8(*b*), agreeing well with all experimental results. The differences in the effects of bubble competition and spike competition on the RM instability can be explained by the different nonlinear behaviours of bubbles and spikes of diverse order modes. For the two-bubble interface, the first-order mode saturates much later than the higher-order modes. Therefore, the suppression of the first-order mode on the short-wavelength bubble becomes dominant,

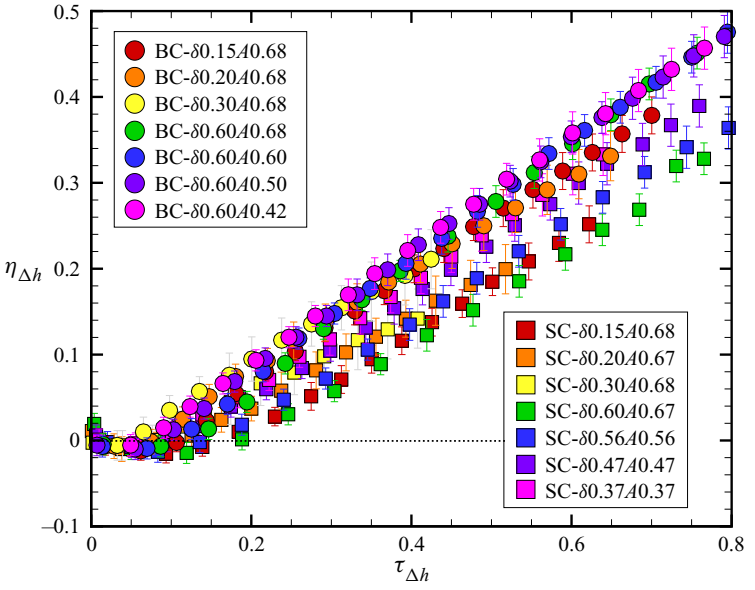

Figure 11. Comparisons of the time-varying height differences between the two bubbles and two spikes in all cases.

even leading to the short-wavelength bubble growing in the opposite direction when δ is large. Differently, for the two-spike interface, all constituent modes maintain a long-time linear growth. As a result, although the first-order mode suppresses the short-wavelength spike growth, the higher-order modes still result in the short-wavelength spike being more unstable.

Last, the height differences between the two bubbles and two spikes (as sketched in figure 7), which are critical parameters for quantifying the effects of bubble competition and spike competition, are discussed in this study. The time-varying height differences (Δh) in all cases are shown in figure 11. Time for the two-bubble/two-spike interface case is scaled as $\tau_{\Delta h} = 2\pi^2 t_{B/S} Z \Delta h^0 \Delta v A/(\lambda_L + \lambda_S)^2$ and height difference is scaled as $\eta_{\Delta h} = \pi(\Delta h - Z\Delta h^0)/(\lambda_L + \lambda_S)$, with Δh^0 denoting the initial height difference and the values of which are listed in table 1. It is found that before a dimensionless criterion time, $\tau^*_{\Delta h}$, the dimensionless Δh remains zero, indicating that the two bubbles and two spikes grow independently. The values of $\tau^*_{\Delta h}$ in all cases are listed in table 1. It is evident that $\tau^*_{\Delta h}$ in two-bubble studies is smaller than in the corresponding two-spike studies, indicating that the bubble-competition effect on the RM instability occurs earlier than its spike-competition counterpart. As A decreases, the differences in $\tau^*_{\Delta h}$ between the two-bubble and two-spike studies become smaller.

Moreover, the dimensionless Δh in the two-spike studies is smaller than in the corresponding two-bubble studies, demonstrating that the bubble-competition effect on the RM instability is stronger than its spike-competition counterpart. As A decreases, the dimensionless Δh in two-spike studies increases significantly and is slightly lower than that in two-bubble studies, indicating that the spike-competition effect becomes stronger, and the effects of bubble competition and spike competition on the RM instability are more similar when the densities of the two fluids are comparable. Overall, bubble competition suppresses the short-wavelength perturbations more than spike competition, especially under conditions of high density ratio. Therefore, the two-bubble configuration is more

desirable in an ICF target design than the two-spike configuration to reduce the mixing of high-frequency perturbations.

5. Conclusions

In this work, various 2-D two-bubble and two-spike interfaces with diverse initial spectra and density ratios are first formed by the extended soap film technique. Then elaborate shock-tube experiments are performed to explore the differences between bubble competition and spike competition. The spike competition in RM flows, which is caused by the different influences of the two-side bubbles on the long-wavelength spike and short-wavelength spike of a two-spike interface, is investigated for the first time.

Compared with the RM instability of a single-mode interface, the bubble competition obviously suppresses the short-wavelength bubble growth, which strongly depends on the initial spectra of the two-bubble configuration and weakly depends on the density ratio. Differently, the suppression of the spike competition on the short-wavelength spike growth is dependent on both the initial spectra and density ratio. Moreover, bubble competition slightly promotes the RM instability of long-wavelength bubbles, while spike competition has a limited influence on the RM instability of long-wavelength spikes.

The buoyancy–drag model is derived to establish a relation between the growth factors for bubbles and spikes and the initial spectra and density ratio. As the size ratio of the long-wavelength structure to the short-wavelength structure, i.e. δ, increases, the drag per unit volume imposed on the short-wavelength bubble and spike increases, but that imposed on the long-wavelength bubble decreases and that imposed on the long-wavelength spike remains unchanged. As the density ratio increases, heavier fluids induce a larger drag force on bubbles while lighter fluids impose a smaller drag force on spikes.

The lowest frequency mode of the initial spectra, i.e. the spanwise flow field, suppresses the short-wavelength structure development, especially when δ is large. The differences between bubble competition and spike competition are ascribed to the different nonlinear behaviours of bubbles and spikes of the constituent modes in RM flows. The bubble-competition effect occurs earlier and is stronger than the spike-competition effect, especially under conditions of high density ratio. As a result, the short-wavelength bubble is suppressed more than the short-wavelength spike. This suggests that one should adopt the two-bubble configuration rather than the two-spike configuration in ICF target design to reduce the mixing of high-frequency perturbations.

Acknowledgements. The authors appreciate the valuable suggestions of the reviewers.

Funding. This work was supported by the Natural Science Foundation of China (nos. 91952205 and 11625211) and Tamkeen under NYU Abu Dhabi Research Institute grant CG002.

Declaration of interests. The authors report no conflict of interest.

Author ORCIDs.
Yu Liang https://orcid.org/0000-0002-3254-7073;
Xisheng Luo https://orcid.org/0000-0002-4303-8290.

References

ABARZHI, S.I. 2008 Coherent structures and pattern formation in Rayleigh–Taylor turbulent mixing. *Phys. Scr.* **78** (1), 015401.

ABARZHI, S.I. 2010 Review of theoretical modelling approaches of Rayleigh–Taylor instabilities and turbulent mixing. *Phil. Trans. R. Soc.* A **368** (1916), 1809–1828.

ALON, U., HECHT, J., MUKAMEL, D. & SHVARTS, D. 1994 Scale invariant mixing rates of hydrodynamically unstable interface. *Phys. Rev. Lett.* **72**, 2867–2870.

ALON, U., HECHT, J., OFER, D. & SHVARTS, D. 1995 Power laws and similarity of Rayleigh–Taylor and Richtmyer-Meshkov mixing fronts. *Phys. Rev. Lett.* **74**, 534–537.

BALASUBRAMANIAN, S., ORLICZ, G.C. & PRESTRIDGE, K.P. 2013 Experimental study of initial condition dependence on turbulent mixing in shock-accelerated Richtmyer-Meshkov fluid layers. *J. Turbul.* **14** (3), 170–196.

BROUILLETTE, M. 2002 The Richtmyer-Meshkov instability. *Annu. Rev. Fluid Mech.* **34**, 445–468.

CAO, Y.G., CHOW, W.K. & FONG, N.K. 2011 Solutions to buoyancy-drag equation for dynamical evolution of Rayleigh–Taylor and Richtmyer-Meshkov mixing zone. *Commun. Theor. Phys.* **56** (4), 751–755.

CHENG, B., GLIMM, J. & SHARP, D.H. 2000 Density dependence of Rayleigh–Taylor and Richtmyer-Meshkov mixing fronts. *Phys. Lett.* A **268**, 366–374.

CHENG, B., GLIMM, J. & SHARP, D.H. 2002 Dynamical evolution of Rayleigh–Taylor and Richtmyer-Meshkov mixing fronts. *Phys. Rev.* E **66**, 036312.

CHENG, B., GLIMM, J. & SHARP, D.H. 2020 The α_s and θ_s in Rayleigh–Taylor and Richtmyer-Meshkov instabilities. *Physica* D **404**, 132356.

DI STEFANO, C.A., MALAMUD, G., KURANZ, C.C., KLEIN, S.R. & DRAKE, R.P. 2015*a* Measurement of Richtmyer-Meshkov mode coupling under steady shock conditions and at high energy density. *High Energy Density Phys.* **17**, 263–269.

DI STEFANO, C.A., MALAMUD, G., KURANZ, C.C., KLEIN, S.R., STOECKL, C. & DRAKE, R.P. 2015*b* Richtmyer-Meshkov evolution under steady shock conditions in the high-energy-density regime. *Appl. Phys. Lett.* **106** (11), 114103.

DIMONTE, G. 2000 Spanwise homogeneous buoyancy-drag model for Rayleigh–Taylor mixing and experimental evaluation. *Phys. Plasmas* **7**, 2255–2269.

DIMONTE, G. & RAMAPRABHU, P. 2010 Simulations and model of the nonlinear Richtmyer-Meshkov instability. *Phys. Fluids* **22**, 014104.

DIMONTE, G. & SCHNEIDER, M. 2000 Density ratio dependence of Rayleigh–Taylor mixing for sustained and impulsive acceleration histories. *Phys. Fluids* **12**, 304–321.

DIMONTE, G., YOUNGS, D.L., DIMITS, A., WEBER, S. & ZINGALE, M. 2004 A comparative study of the turbulent Rayleigh–Taylor instability using high-resolution three-dimensional numerical simulations: the alpha-group collaboration. *Phys. Fluids* **16** (5), 1668–1693.

DRAKE, R.P. 2018 *High-Energy-Density Physics: Foundation of Inertial Fusion and Experimental Astrophysics*. Springer.

ELBAZ, Y. & SHVARTS, D. 2018 Modal model mean field self-similar solutions to the asymptotic evolution of Rayleigh–Taylor and Richtmyer-Meshkov instabilities and its dependence on the initial conditions. *Phys. Plasmas* **25** (6), 062126.

GROOM, M. & THORNBER, B. 2020 The influence of initial perturbation power spectra on the growth of a turbulent mixing layer induced by Richtmyer-Meshkov instability. *Physica* D **407**, 132463.

GUO, X., ZHAI, Z., SI, T. & LUO, X. 2019 Bubble merger in initial Richtmyer-Meshkov instability on inverse-chevron interface. *Phys. Rev. Fluids* **4** (9), 092001.

HAAN, S.W. 1991 Weakly nonlinear hydrodynamic instabilities in inertial fusion. *Phys. Fluids* B **3**, 2349–2355.

HECHT, J., ALON, U. & SHVARTS, D. 1994 Potential flow models of Rayleigh–Taylor and Richtmyer-Meshkov bubble fronts. *Phys. Fluids* **6**, 4019–4030.

JACOBS, J.W. & KRIVETS, V.V. 2005 Experiments on the late-time development of single-mode Richtmyer-Meshkov instability. *Phys. Fluids* **17**, 034105.

JACOBS, J.W. & SHEELEY, J.M. 1996 Experimental study of incompressible Richtmyer-Meshkov instability. *Phys. Fluids* **8**, 405–415.

KURANZ, C.C., *et al.* 2018 How high energy fluxes may affect Rayleigh–Taylor instability growth in young supernova remnants. *Nat. Commun.* **9**, 1564.

LAYZER, D. 1955 On the instability of superposed fluids in a gravitational field. *Astrophys. J.* **122**, 1–12.

LIANG, Y. 2022 *Fundamental Studies of Shock-Driven Hydrodynamic Instabilities*. Springer Nature Singapore.

LIANG, Y., LIU, L., ZHAI, Z., DING, J., SI, T. & LUO, X. 2021*a* Richtmyer-Meshkov instability on two-dimensional multi-mode interfaces. *J. Fluid Mech.* **928**, A37.

LIANG, Y., LIU, L., ZHAI, Z., SI, T. & LUO, X. 2021*b* Universal perturbation growth of Richtmyer-Meshkov instability for minimum-surface featured interface induced by weak shock waves. *Phys. Fluids* **33** (3), 032110.

LIANG, Y., ZHAI, Z., DING, J. & LUO, X. 2019 Richtmyer-Meshkov instability on a quasi-single-mode interface. *J. Fluid Mech.* **872**, 729–751.

LINDL, J., LANDEN, O., EDWARDS, J., MOSES, E. & TEAM, N. 2014 Review of the national ignition campaign 2009–2012. *Phys. Plasmas* **21**, 020501.

LIU, L., LIANG, Y., DING, J., LIU, N. & LUO, X. 2018 An elaborate experiment on the single-mode Richtmyer-Meshkov instability. *J. Fluid Mech.* **853**, R2.

LIVESCU, D. 2020 Turbulence with large thermal and compositional density variations. *Annu. Rev. Fluid Mech.* **52**, 309–341.

LOMBARDINI, M. & PULLIN, D.I. 2009 Startup process in the Richtmyer-Meshkov instability. *Phys. Fluids* **21** (4), 044104.

LUO, X., LIANG, Y., SI, T. & ZHAI, Z. 2019 Effects of non-periodic portions of interface on Richtmyer-Meshkov instability. *J. Fluid Mech.* **861**, 309–327.

LUO, X., LIU, L., LIANG, Y., DING, J. & WEN, C.Y. 2020 Richtmyer-Meshkov instability on a dual-mode interface. *J. Fluid Mech.* **905**, A5.

MANSOOR, M.M., DALTON, S.M., MARTINEZ, A.A., DESJARDINS, T., CHARONKO, J.J. & PRESTRIDGE, K.P. 2020 The effect of initial conditions on mixing transition of the Richtmyer-Meshkov instability. *J. Fluid Mech.* **904**, A3.

MARIANI, C., VANDENBOOMGAERDE, M., JOURDAN, G., SOUFFLAND, D. & HOUAS, L. 2008 Investigation of the Richtmyer-Meshkov instability with stereolithographed interfaces. *Phys. Rev. Lett.* **100**, 254503.

MESHKOV, E.E. 1969 Instability of the interface of two gases accelerated by a shock wave. *Fluid Dyn.* **4**, 101–104.

MIKAELIAN, K.O. 1989 Turbulent mixing generated by Rayleigh–Taylor and Richtmyer-Meshkov instabilities. *Physica* D **36**, 343–357.

MILES, A.R., EDWARDS, M.J., BLUE, B., HANSEN, J.F., ROBEY, H.F., DRAKE, R.P., KURANZ, C. & LEIBRANDT, D.R. 2004 The effects of a short-wavelength mode on the evolution of a long-wavelength perturbatoin driven by a strong blast wave. *Phys. Plasmas* **11**, 5507–5519.

MOHAGHAR, M., CARTER, J., PATHIKONDA, G. & RANJAN, D. 2019 The transition to turbulence in shock-driven mixing: effects of Mach number and initial conditions. *J. Fluid Mech.* **871**, 595–635.

NIEDERHAUS, C.E. & JACOBS, J.W. 2003 Experimental study of the Richtmyer-Meshkov instability of incompressible fluids. *J. Fluid Mech.* **485**, 243–277.

NISHIHARA, K., WOUCHUK, J.G., MATSUOKA, C., ISHIZAKI, R. & ZHAKHOVSKY, V.V. 2010 Richtmyer-Meshkov instability: theory of linear and nonlinear evolution. *Phil. Trans. R. Soc.* A **368**, 1769–1807.

OFER, D., ALON, U., SHVARTS, D., MCCRORY, R.L. & VERDON, C.P. 1996 Modal model for the nonlinear multimode Rayleigh–Taylor instability. *Phys. Plasmas* **3** (8), 3073–3090.

ORON, D., ARAZI, L., KARTOON, D., RIKANATI, A., ALON, U. & SHVARTS, D. 2001 Dimensionality dependence of the Rayleigh–Taylor and Richtmyer-Meshkov instability late-time scaling laws. *Phys. Plasmas* **8**, 2883–2889.

PANDIAN, A., STELLINGWERF, R.F. & ABARZHI, S.I. 2017 Effect of a relative phase of waves constituting the initial perturbation and the wave interference on the dynamics of strong-shock-driven Richtmyer-Meshkov flows. *Phys. Rev. Fluids* **2** (7), 073903.

RAMAPRABHU, P., DIMONTE, G. & ANDREWS, M.J. 2005 A numerical study of the influence of initial perturbations on the turbulent Rayleigh–Taylor instability. *J. Fluid Mech.* **536**, 285–319.

RANJAN, D., OAKLEY, J. & BONAZZA, R. 2011 Shock-bubble interactions. *Annu. Rev. Fluid Mech.* **43**, 117–140.

RAYLEIGH, LORD 1883 Investigation of the character of the equilibrium of an incompressible heavy fluid of variable density. *Proc. London Math. Soc.* **14**, 170–177.

RICHTMYER, R.D. 1960 Taylor instability in shock acceleration of compressible fluids. *Commun. Pure Appl. Maths* **13**, 297–319.

RIKANATI, A., ALON, U. & SHVARTS, D. 1998 Vortex model for the nonlinear evolution of the multimode Richtmyer-Meshkov instability at low Atwood numbers. *Phys. Rev.* E **58**, 7410–7418.

SADOT, O., EREZ, L., ALON, U., ORON, D., LEVIN, L.A., EREZ, G., BEN-DOR, G. & SHVARTS, D. 1998 Study of nonlinear evolution of single-mode and two-bubble interaction under Richtmyer-Meshkov instability. *Phys. Rev. Lett.* **80**, 1654–1657.

SHARP, D.H. 1984 An overview of Rayleigh–Taylor instability. *Physica* D **12** (1), 3–18.

SREBRO, Y., ELBAZ, Y., SADOT, O., ARAZI, L. & SHVARTS, D. 2003 A general buoyancy-drag model for the evolution of the Rayleigh–Taylor and Richtmyer-Meshkov instabilities. *Laser Part. Beams* **21**, 347–353.

TAYLOR, G. 1950 The instability of liquid surfaces when accelerated in a direction perpendicular to their planes. I. *Proc. R. Soc. Lond.* A **201** (1065), 192–196.

THORNBER, B. 2016 Impact of domain size and statistical errors in simulations of homogeneous decaying turbulence and the Richtmyer-Meshkov instability. *Phys. Fluids* **28** (4), 045106.

THORNBER, B., DRIKAKIS, D., YOUNGS, D.L. & WILLIAMS, R.J.R. 2010 The influence of initial condition on turbulent mixing due to Richtmyer-Meshkov instability. *J. Fluid Mech.* **654**, 99–139.

THORNBER, B., *et al.* 2017 Late-time growth rate, mixing, and anisotropy in the multimode narrowband Richtmyer-Meshkov instability: the θ-group collaboration. *Phys. Fluids* **29** (10), 105107.

VANDENBOOMGAERDE, M., GAUTHIER, S. & MÜGLER, C. 2002 Nonlinear regime of a multimode Richtmyer-Meshkov instability: a simplified perturbation theory. *Phys. Fluids* **14** (3), 1111–1122.

VANDENBOOMGAERDE, M., SOUFFLAND, D., MARIANI, C., BIAMINO, L., JOURDAN, G. & HOUAS, L. 2014 An experimental and numerical investigation of the dependency on the initial conditions of the Richtmyer-Meshkov instability. *Phys. Fluids* **26**, 024109.

VELIKOVICH, A.L. & DIMONTE, G. 1996 Nonlinear perturbation theory of the incompressible Richtmyer-Meshkov instability. *Phys. Rev. Lett.* **76** (17), 3112.

VELIKOVICH, A., HERRMANN, M. & ABARZHI, S. 2014 Perturbation theory and numerical modelling of weakly and moderately nonlinear dynamics of the incompressible Richtmyer-Meshkov instability. *J. Fluid Mech.* **751**, 432–479.

WADAS, M.J. & JOHNSEN, E. 2020 Interactions of two bubbles along a gaseous interface undergoing the Richtmyer-Meshkov instability in two dimensions. *Physica* D **409**, 132489.

YANG, J., KUBOTA, T. & ZUKOSKI, E.E. 1993 Application of shock-induced mixing to supersonic combustion. *AIAA J.* **31**, 854–862.

YOUNGS, D.L. 1991 Numerical simulation of turbulent mixing by Rayleigh–Taylor instability. *Physica* D **12** (1–3), 32–44.

YOUNGS, D.L. 2013 The density ratio dependence of self-similar Rayleigh–Taylor mixing. *Phil. Trans. R. Soc.* A **371**, 20120173.

YOUNGS, D.L. & THORNBER, B. 2020 Buoyancy-drag modelling of bubble and spike distances for single-shock Richtmyer-Meshkov mixing. *Physica* D **410**, 132517.

ZHAI, Z., ZOU, L., WU, Q. & LUO, X. 2018 Review of experimental Richtmyer-Meshkov instability in shock tube: from simple to complex. *Proc. Inst. Mech. Engng, Part* C **232**, 2830–2849.

ZHANG, Q., DENG, S. & GUO, W. 2018 Quantitative theory for the growth rate and amplitude of the compressible Richtmyer-Meshkov instability at all density ratios. *Phys. Rev. Lett.* **121** (17), 174502.

ZHANG, Q. & GUO, W. 2016 Universality of finger growth in two-dimensional Rayleigh–Taylor and Richtmyer-Meshkov instabilities with all density ratios. *J. Fluid Mech.* **786**, 47–61.

ZHANG, Q. & SOHN, S.I. 1997 Nonlinear theory of unstable fluid mixing driven by shock wave. *Phys. Fluids* **9**, 1106–1124.

ZHOU, Y. 2017*a* Rayleigh–Taylor and Richtmyer-Meshkov instability induced flow, turbulence, and mixing. I. *Phys. Rep.* **720–722**, 1–136.

ZHOU, Y. 2017*b* Rayleigh–Taylor and Richtmyer-Meshkov instability induced flow, turbulence, and mixing. II. *Phys. Rep.* **723–725**, 1–160.

ZHOU, Y., CLARK, T.T., CLARK, D.S., GLENDINNING, S.S., SKINNER, A.A., HUNTINGTON, C., HURRICANE, O.A., DIMITS, A.M. & REMINGTON, B.A. 2019 Turbulent mixing and transition criteria of flows induced by hydrodynamic instabilities. *Phys. Plasmas* **26** (8), 080901.

ZHOU, Y., *et al.* 2021 Rayleigh–Taylor and Richtmyer-Meshkov instabilities: a journey through scales. *Physica* D **423**, 132838.

ZHOU, Z.R., ZHANG, Y.S. & TIAN, B.L. 2018 Dynamic evolution of Rayleigh–Taylor bubbles from sinusoidal, w-shaped, and random perturbations. *Phys. Rev.* E **97** (3), 033108.